

Comparison of mid-infrared laser diode active regions

J. T. Olesberg^a, Michael E. Flatté^a, B. J. Brown^a, T. C. Hasenberg^a, S. A. Anson^a, Thomas F. Boggess^a,
and C. H. Grein^b

^aThe University of Iowa, Iowa City, IA

^bThe University of Illinois at Chicago, Chicago, IL

ABSTRACT

The development of mid-infrared interband diode lasers has been hindered by factors such as Auger recombination and intervalence band absorption, which become increasingly important at longer wavelengths. A number of structures have been proposed in which the effects of these processes are reduced. The maximum gain per unit volumetric current density can be used as a figure of merit for comparing different active region materials. Using this figure of merit, we compare a series of structures with band gaps near 0.3 eV (i.e., wavelengths near 4 microns). The figure of merit is obtained from gain spectra calculated using superlattice **K-p** theory and a combination of calculated and measured recombination rates. We show that devices based on active regions incorporating type-I InAsSb/AlInAsSb or InAsSb/InAsP quantum wells should have room temperature threshold currents 7-13 times smaller than those of devices based on bulk InAs. However, devices using type-II superlattice active regions should have room temperature threshold currents that are a factor of 3-4 times smaller than those of the type-I quantum wells. The figure of merit can also be used to determine the optimal thickness of the active region as a function of waveguide loss and optical mode width.

Keywords: laser diode, semiconductor laser, mid-infrared, Auger recombination, quantum well, superlattice

1. INTRODUCTION

Active regions in current III-V semiconductor lasers emitting in the mid-infrared wavelength range (3-5 μm) have been grown from a wide variety of material systems. There are type-I interband lasers, such as InAsSb/AlAsSb,¹ InAsSb/InAsP,² or InSb/AlInSb;³ type-II broken gap lasers, either in traditional^{4,5} or cascade⁶ configuration; and intersubband cascade lasers.⁷ A variety of claims have been made concerning the relative ideal performance of the systems, but most involve a few specific properties of the active region, such as the Auger coefficient or differential gain. It is better to compare active regions using a figure of merit that includes and properly weighs all of the relevant properties. Such a figure of merit, the net active region gain per unit volumetric current, has been used previously in the context of near-infrared laser diode development.⁸ In this proceedings, we use this figure of merit to compare a number of non-cascaded mid-infrared active regions.

The primary limitation in present high-temperature mid-infrared laser diode operation is device heating due to the applied current and voltage. The appropriate figure of merit is obtained by minimizing the required ohmic power for a given output optical power. For non-cascade laser diodes, it can be assumed that operating voltages are comparable, and we seek to minimize the required current density for a given output power. The required external current density can be written

$$\frac{I}{A} = \frac{D_{mode}(\alpha_m + \langle \alpha_w \rangle)}{\eta_i} \left[\frac{J}{\gamma - \alpha_a} \right] + \frac{1}{\eta_i} \frac{1}{A} \frac{eP_0}{h\nu} \frac{\alpha_m + \langle \alpha_w \rangle}{\alpha_m} \left[\frac{\gamma}{\gamma - \alpha_a} \right] \quad (1)$$

where I is the total current applied to the leads, A is the stripe area (length time width), η_i is the internal quantum efficiency, α_a is the optical loss in the active region (due, for example, to intervalence band absorption), α_m is the mirror reflectivity loss, and $\langle \alpha_w \rangle$ is the modal waveguide loss (losses not associated with the active region or the mirrors). D_{mode} is a measure of the optical mode width and is defined by $D_{mode} \equiv D/\Gamma$, where D is the active region thickness and Γ is the overlap of the optical mode with the active region. J is the volumetric current density in the

active region required to produce material gain γ , e is the fundamental charge, P_0 is the output optical power, and $h\nu$ is the photon energy. The first term of equation (1) describes the current density required to maintain the diode at threshold and the second term describes the current density above threshold necessary to obtain the desired optical power.

In both the threshold and output power terms of equation (1) the variables related to the active region (shown in square braces) can be isolated. The inverse of these terms can be used as figures of merit for optimizing laser diode operation and for comparing different active region materials. The figure of merit for minimizing the threshold current density is the maximum of the net material gain per volumetric current density in the active region, $[(\gamma - \alpha_a)/J]_{max}$,⁸ while the figure of merit for maximizing the slope efficiency is the maximum of the net material gain per fundamental gain, $[(\gamma - \alpha_a)/\gamma]_{max}$.⁹ Both of these figures of merit are intensive material quantities that do not depend on the geometry of the active region or cavity. Because of this, these figures of merit can be used to compare bulk, quantum well, or superlattice active regions in a device-independent, head-to-head fashion. The threshold figure of merit includes and properly weighs the impact of lasing transition strengths, Auger recombination, intersubband absorption, differential gain, gain saturation, and the balancing and reduction of the valence and conduction densities of states. The slope efficiency figure of merit measures the impact of intersubband absorption and gain saturation on high-power operation.

Evaluation of these figures of merit and knowledge of the active region density at which the maxima occur allows us to determine the optimum active region thickness as a function of mode width and modal loss. For a separate confinement structure, where the mode width and waveguide losses are roughly independent of the active region thickness, the active region can be optimized independently of the waveguide. For a double-heterostructure, however, it is necessary to balance optimization of the active region with optimization of the waveguide.

The rationale behind the traditional approach of thick active regions for interband lasers has been that the rapid increase of Auger recombination with carrier density makes high-density operation of the active region unfavorable. This argument has also been suggested as a motivation for cascade structures. Recent 2 μm lasers based on active region with a few quantum wells, however, have produced high powers and operating temperatures. A five quantum well active region operated continuous-wave (CW) at room temperature with a differential efficiency of 36%,¹⁰ while a single quantum well active region produced 1.9 W of CW power at room temperature with a differential efficiency of 53%.¹¹ Similar structures have been grown which lased near room temperature at 2.7 μm . In view of this success, we reconsider the issue of the optimal thickness of the active region materials in 4 μm lasers. For active region materials with the highest net gain to current density ratio, we find that the optimal thicknesses are much thinner than are commonly grown.

We report calculations of the maximum net gain per unit current density, the ratio of net gain to fundamental gain, optimal active region thicknesses, and threshold current densities for six active region systems at room temperature. These include bulk InAs, a 4.4 μm InAs_{0.0.88}Sb_{0.12}/InAs_{0.76}P_{0.24} strained quantum well,² a 4.0 μm InAs_{0.85}Sb_{0.15}/Al_{0.13}In_{0.87}As_{0.91}Sb_{0.09} strained quantum well,¹² a 4.0 μm InAs/Ga_{0.60}In_{0.40}Sb/InAs/Al_{0.30}Ga_{0.42}In_{0.28}As_{0.50}Sb_{0.50} superlattice,¹³ a 4.0 μm InAs/Ga_{0.70}In_{0.30}Sb/InAs/AlSb superlattice,⁵ and a recently proposed 3.4 μm broken-gap quantum well. The broken-gap quantum well, which is designed specifically for electrical injection, consists of an AlAsSb/InAs/GaInSb/InAs/AlAsSb well surrounded by AlGaSb/InAs superlattice barriers. Details on this structure will be provided in a future publication.¹⁴

2. CALCULATION PROCEDURE

Calculation of the gain and intersubband absorption spectra is performed with the full nonparabolic band structure and momentum-dependent matrix elements obtained from a 14-band bulk basis superlattice $\mathbf{K}\cdot\mathbf{p}$ formalism similar to Ref. 15 but with a larger bulk basis and generalized to an arbitrary number of superlattice layers. Input parameters to the calculation are limited to the zone center matrix elements between the bulk states and the

strained bulk band-edge energies. The matrix elements for each bulk constituent were linearly interpolated from bulk binary values, which were determined from fitting available bulk effective masses and Landé g -factors taken from Ref. 16. This superlattice $\mathbf{K}\cdot\mathbf{p}$ formalism has been very successful in calculating the optical properties of related type-II multilayer structures.¹⁷

Density-dependent recombination rates were calculated using $J = neR(n)$, where n ($=p$) is the active region carrier density and $R(n)$ is the per-carrier recombination rate. A Shockley-Read-Hall (SRH) lifetime of 3 ns was used for all of the structures. A single value is used for all of the materials since the SRH lifetime is not an intrinsic material property. At room temperature, the SRH recombination rate is insignificant compared to the Auger rate for most of the systems considered. Room temperature radiative recombination rates were calculated using the superlattice $\mathbf{K}\cdot\mathbf{p}$ formalism and are typically much smaller than the SRH rate.

Experimental Auger recombination rates were used when available. When they were not, rates were determined by means of a Golden rule calculation using the non-parabolic band structure. The transition matrix elements used for the Auger calculation are evaluated using a statically screened Coulomb interaction and first-order $\mathbf{K}\cdot\mathbf{p}$ perturbation theory for the wave function overlaps. Details of the Auger formalism are available in Refs. 18 and 19. Only direct Auger processes are considered in the calculation. In the case of system V, which has been studied in detail, the calculated Auger rates and the experimental Auger rates agree within experimental error (25%).²⁰

Recombination rate information used to calculate the volumetric current density is detailed in Table 1. For most of the systems, the Auger rate per electron-hole pair can be written $R_{Auger}(n) = Cn^2$, where C the Auger coefficient. For systems V and VI, however, the Auger rate becomes linear with density at high densities and cannot be fit with a simple quadratic.²⁰ The rate can be fit with the form

$$R_{Auger}(n) = Cn^2 / (1 + n / n_{sat}) \quad (2)$$

where n_{sat} is the density at which the rate is one-half of what it would be without saturation. The deviation from the normal quadratic density dependence is due to the impact of degeneracy in the valence band.

	System	E_g (μm)	C ($10^{-27} \text{ cm}^6/\text{s}$)	n_{sat} (10^{17} cm^{-3})	Origin
I	<i>BULK</i> InAs	3.5	11	-	ultrafast pump-probe, Ref. 21
II	<i>QUANTUM WELLS</i> InAsSb / InAsP	4.4	13.4	-	calculated
III	InAsSb / AlInAsSb	3.8	9.0	-	pulsed photoconductivity, Ref. 12
	<i>SUPERLATTICES</i>				
IV	InAs / GaInSb / InAs / AlSb	4.0	3.4	-	calculated
V	InAs / GaInSb / InAs / AlGaInAsSb	4.0	2.9	35	ultrafast pump-probe, Ref. 22
	<i>BROKEN-GAP</i>				
VI	<i>QUANTUM WELL</i> InAs / GaInSb / InAs	3.4	2.1	2	calculated

Table 1: Room temperature Auger recombination rate information for the six mid-infrared material systems considered. When a saturation density, n_{sat} , is shown, the Auger rate as a function of density is described by the saturated form shown in equation (2). The Auger coefficients for the quantum well samples are based on densities calculated with the convention that the entire MQW period is used for the growth-direction length, rather than just the quantum well width.

We note that the value of the Auger coefficient depends on the growth-direction length used to calculate volumetric density. Some authors use the quantum well width as the growth-direction length scale; others prefer to use the entire period of the multiple quantum well (MQW) or superlattice. We use the latter convention since some of our work involves type-II superlattices where the conduction and valence wells have different widths and some of the carriers are distributed throughout the entire period of the structure. The Auger coefficient will typically change by a factor of 4-10 depending on which convention is used.

3. RESULTS

The net gain per unit current density is shown as a function of carrier density in Fig. 1 for systems I, II, V, and VI. For each system, $(\gamma - \alpha_a)/J$ is zero at transparency. At high carrier densities, $(\gamma - \alpha_a)/J$ approaches zero since the fundamental gain saturates, intersubband absorption increases, and the recombination current (dominated by Auger recombination) increases dramatically. Between these two extremes, there is an optimal operation point for the active region where the net gain per unit current density is the largest and the threshold current density is minimized. In the case of system VI, this point occurs at a density of $3.5 \times 10^{17} \text{ cm}^{-3}$, which is roughly twice the transparency density.

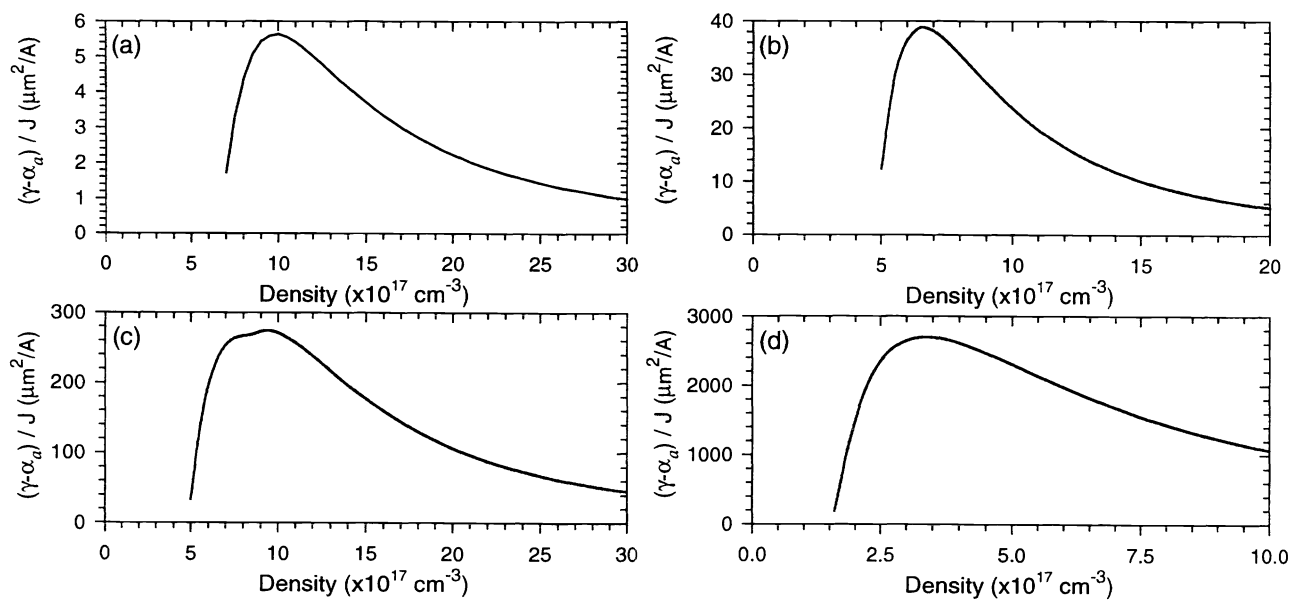


Fig. 1: Net gain per unit volumetric current density, $(\gamma - \alpha_a)/J$, as a function of carrier density for (a) system I, (b) system II, (c) system V, and (d) system VI. Note the different scales. Regardless of the laser cavity design, the active region should be operated at a density near the optimum point to obtain the lowest threshold current density.

The maximum ratio of the net gain to volumetric current density, $[(\gamma - \alpha_a)/J]_{max}$, is shown in Table 2 for each system along with the corresponding net material gain, $(\gamma - \alpha_a)_{opt}$, and carrier density, n_{opt} . We see that the range of values extends over more than factor of 50. The type-I quantum wells have a figure of merit 7-13 time larger than that of bulk InAs. The improvement is primarily due to reduction of the valence band density of states through the use of strain and quantum confinement. Reduction of the valence band density of states helps balance the magnitudes of the conduction and valence band densities of states. The improved balancing of the densities of states reduces the threshold carrier density, increases the differential gain, and helps suppress Auger recombination. A measure of the imbalance between the valence and conduction band densities of states is shown in Table 2 as ρ_v / ρ_c .²³

	System	E_g (μm)	$[(\gamma - \alpha_a) / J]_{max}$ ($\mu\text{m}^2/\text{A}$)	ρ_v / ρ_c	$(\gamma - \alpha_a)_{opt}$ (cm^{-1})	n_{opt} (10^{17}cm^{-3})	D_{opt} (μm)	$\eta_i(I/A)_{th}$ (kA/cm^2)
I	<i>BULK</i> InAs	3.5	5.6	23	102	10	1960	35.7
II	<i>QUANTUM WELLS</i> InAsSb / InAsP	4.4	39	8.1	242	6.5	826	5.13
III	InAsSb / AlInAsSb	3.8	75	9.8	116	4.5	1720	2.67
IV	<i>SUPERLATTICES</i> InAs / GaInSb / InAs / AlSb	4.0	257	2.0	692	7.5	289	0.78
V	InAs / GaInSb / InAs / AlGaInAsSb	4.0	274	2.4	998	9.5	200	0.73
VI	<i>BROKEN-GAP</i> <i>QUANTUM WELL</i> InAs / GaInSb / InAs	3.4	2700	1.6	625	3.4	320	0.074

Table 2: Room temperature results for ideal laser active region designs for the six systems considered: maximum values of the net gain per unit volumetric current density $[(\gamma - \alpha_a) / J]_{max}$, ratio of the valence and conduction band densities of states ρ_v / ρ_c , and the material gain and carrier density that correspond the optimum operating point. The optimal active region thickness, D_{opt} , and the internal threshold current density, $\eta_i(I/A)_{th}$, are calculated assuming $D_{mode} = 20 \text{ cm}^{-1}$ and $\alpha_m - \langle \alpha_w \rangle = 10 \text{ cm}^{-1}$.

The type-II superlattices have a figure of merit 3-7 times larger than that of the type-I quantum wells. The improvement is due to two factors. First, the large valence band offsets of the InAs/GaInSb/InAs system (e.g., 660 meV for system V compared to 150 meV for system III) permit a reduction of the ratio of densities of states by another factor of four. Second, the large valence band offsets make it is possible to create gaps in the electronic band states one energy gap below the top of the valence band. These gaps in the energy spectrum can be used to eliminate final states for intervalenceband absorption and hole-hole Auger recombination processes.¹³ The improved performance of the superlattices over the type-I quantum wells comes in spite of the smaller lasing transition strengths due to the type-II nature of the superlattices. The broken-gap quantum well system takes these same optimizations one step further by reducing the valence band density of states even more. In addition, Auger recombination is further suppressed by the use of a wider final-state gap within the well's valence band electronic structure.¹⁴

Having determined the optimal operating density for each of the systems, the optimal active region thickness can be calculated by requiring that threshold occur at the density (and hence, gain) that correspond to $[(\gamma - \alpha_a) / J]_{max}$.

This means that

$$D_{opt} = D_{mode} \frac{\alpha_m + \langle \alpha_w \rangle}{(\gamma - \alpha_a)_{opt}}. \quad (3)$$

Optimal active region thicknesses are shown in Table 2 for a representative low-loss mid-infrared laser with a separate confinement region and coated facets: $D_{mode} = 2 \mu\text{m}$ and $\alpha_m + \langle \alpha_w \rangle = 10 \text{ cm}^{-1}$. Optimal thicknesses can be readily calculated for different waveguide parameters given the information in Table 2. We find that the optimal active region thickness of the four-layer superlattices are on the order of 3 periods, while the optimal thickness for

the 3.4 μm broken-gap quantum well is a single period. The use of such thin active regions necessitates a separate confinement structure to adequately confine the optical mode and minimize optical losses in the doped clads.

Room temperature threshold current densities are shown in Table 2 for the same waveguide parameters. The threshold densities are inversely proportional to the threshold current density figure of merit. For system VI, we predict an extremely low internal current density of 74 A/cm² due to the highly optimized qualities of the active region.

The preceding discussion has been focused on minimizing threshold current densities. For high-power applications, the effect of the active region on the slope efficiency should also be taken into account. As mentioned previously, the ratio of the net to fundamental material gain of the active region, $(\gamma - \alpha_a)/\gamma$, describes the impact of intersubband absorption within the active region on the slope efficiency. Ratios less than 1.0 indicate that intersubband absorption in the active region is reducing the slope efficiency. Listed in Table 3 are the maximum values of this ratio and the ratio at the carrier density that minimizes the threshold current density, n_{opt} . For systems I-IV, intersubband absorption reduces the slope efficiency by 10-34%. Systems V-VI exhibit better intersubband absorption optimizations, so that the slope efficiency is essentially the value determined by the mirror and modal waveguide losses. For all of the systems other than system II, the ratio of the net to fundamental material gain at n_{opt} is nearly its maximum value. This suggests that, except when intersubband absorption is significant, it is sufficient to minimize the threshold carrier density. It also underscores the importance of suppressing intersubband absorption for high-power devices.

	System	E_g (μm)	$[(\gamma - \alpha_a)/\gamma]_{max}$	$[(\gamma - \alpha_a)/\gamma]_{opt}$
I	<i>BULK</i> InAs	3.5	0.90	0.89
II	<i>QUANTUM WELLS</i> InAsSb / InAsP	4.4	0.76	0.66
III	InAsSb / AlInAsSb	3.8	0.82	0.77
IV	<i>SUPERLATTICES</i> InAs / GaInSb / InAs / AlSb	4.0	0.90	0.86
V	InAs / GaInSb / InAs / AlGaInAsSb	4.0	0.97	0.96
VI	<i>BROKEN-GAP</i> <i>QUANTUM WELL</i> InAs / GaInSb / InAs	3.4	0.99	0.99

Table 3: Effect of intersubband absorption on the slope efficiency: $[(\gamma - \alpha_a)/\gamma]_{max}$ is the maximum slope efficiency multiplier for any density and $[(\gamma - \alpha_a)/\gamma]_{opt}$ is the slope efficiency multiplier at the operating density that minimizes the threshold current density.

There are two quantities of importance to laser diode design which are not represented by the figures of merit. These are the susceptibility to filamentation and vertical mobility of carriers. We have calculated the linewidth enhancement factor for one of the optimized superlattices, system V, which is a measure of susceptibility to filamentation. The value of the linewidth enhancement factor at the density which minimizes the threshold current density is 0.92. This is very close to the minimum linewidth enhancement factor at any density, which is 0.89. The reason for the similarity is that the threshold figure of merit and the linewidth enhancement factor depend on many of the same factors: most notably, the differential gain and the balancing of the densities of states. Therefore, optimized laser active region thicknesses that minimize the threshold current density should be near the thicknesses that minimize the susceptibility to filamentation as well.

The issue of vertical mobility is of particular importance for type-II superlattices similar to systems IV and V due to their large valence band offsets. However, small vertical mobilities are less of a problem when thin active regions are used (2-5 periods). Formerly, a 2.7 μm laser diode grown as an unoptimized double heterostructure with 40 periods of a superlattice similar to system V lased under electrical injection up to 180 K. We expect diodes with thinner active regions and optimized waveguides to operate at higher temperatures and longer wavelengths.

4. CONCLUSIONS

We have compared six mid-infrared active regions at room temperature using two active-region figures of merit obtained from minimizing the applied ohmic power necessary to achieve a specified optical power. The first figure of merit, which minimizes the threshold current density, is the ratio of the net gain per unit volumetric current density in the active region, $(\gamma - \alpha_a)/J$. The figure of merit that minimizes the effect of loss in the active region on the slope efficiency is the ratio of the net material gain to the fundamental material gain, $(\gamma - \alpha_a)/\gamma$. We see that the type-I quantum wells considered should have room temperature current densities that are a factor of 7-13 times smaller than bulk InAs. Four-layer, type-II superlattices should further reduce threshold current densities by a factor of 3-4. Finally, a recently proposed quantum well structure based on a InAs/GaInSb/InAs well should have threshold current densities nearly an order of magnitude smaller than the four-layer superlattices. Optimal active region thicknesses for the type-II materials are \sim 1-4 periods, which is much thinner than has been grown.

5. ACKNOWLEDGEMENTS

This research was supported in part by the U.S. Air Force Materiel Command, Air Force Research Laboratory, Kirtland AFB, New Mexico 87117-5777 (Contract No. F29601-97-C-0041) and the National Science Foundation (Grant No. ECS-9707799).

6. REFERENCES

- ¹ H. K. Choi, G. W. Turner, and M. J. Manfra, "High CW power (>200 mW/facet) at 3.4 μm from InAsSb/InAlAsSb strained quantum well diode lasers," *Electron. Lett.* **32**, pp. 1296-1297, 1996; H. K. Choi, G. W. Turner, M. J. Manfra, and M. K. Connors, "175 K continuous wave operation of InAsSb/InAlAsSb quantum-well diode lasers emitting at 3.5 μm ," *Appl. Phys. Lett.* **68**, pp. 2936-2938, 1996.
- ² S. R. Kurtz, A. A. Allerman, and R. M. Biefeld, "Mid-infrared lasers and light-emitting diodes with InAsSb/InAsP strained-layer superlattice active regions," *Appl. Phys. Lett.* **70**, pp. 3188-3190, 1997.
- ³ T. Ashley, C. T. Elliot, R. Jefferies, A. D. Johnson, G. J. Pryce, A. M. White, and M. Carroll, "Mid-infrared $\text{In}_{1-x}\text{Al}_x\text{Sb}/\text{InSb}$ heterostructure diode lasers," *Appl. Phys. Lett.* **70**, pp. 931-933, 1997.
- ⁴ D. H. Chow, R. H. Miles, T. C. Hasenberg, A. R. Kost, Y. H. Zhang, H. L. Dunlap, and L. West, "Mid-wave infrared diode lasers based on GaInSb/InAs and InAs/AlSb superlattices," *Appl. Phys. Lett.* **67**, pp. 3700-3702, 1995; T. C. Hasenberg, D. H. Chow, A. R. Kost, R. H. Miles, and L. West, "Demonstration of 3.5 μm $\text{Ga}_{1-x}\text{In}_x\text{Sb}/\text{InAs}$ superlattice diode laser," *Electron. Lett.* **31**, pp. 275-276, 1995; T. C. Hasenberg, R. H. Miles, A. R. Kost, and L. West, "Recent advances in Sb-based Midwave-infrared lasers," *IEEE J. Quantum Electron.* **33**, pp. 1403-1406, 1997.
- ⁵ J. I. Malin, J. R. Meyer, C. L. Felix, J. R. Lindle, L. Goldberg, C. A. Hoffman, and F. J. Bartoli, "Type II mid-infrared quantum well lasers," *Appl. Phys. Lett.* **68**, pp. 2976-2978, 1996.
- ⁶ L. J. Olafsen, E. H. Aifer, I. Vurgaftman, W. W. Bewley, C. L. Felix, J. R. Meyer, D. Zhang, C.-H. Lin, and S. S. Pei, "Near-room-temperature mid-infrared interband cascade laser," *Appl. Phys. Lett.* **72**, pp. 2370-2372, 1998.
- ⁷ Jérôme Faist, Federico Capasso, Deborah L. Sivco, Albert L. Hutchinson, Sung-Nee G. Chu, and Alfred Y. Cho, "Short wavelength ($\lambda \sim 3.4$ μm) quantum cascade laser based on strained compensated InGaAs/AlInAs," *Appl. Phys. Lett.* **72**, pp. 680-682, 1998; Jérôme Faist, Alessandro Tredicucci, Federico Capasso, Carlo Sirtori, Deborah L. Sivco, James N. Baillargeon, Albert L. Hutchinson, and Alfred Y. Cho, "High-power continuous-wave quantum cascade lasers," *IEEE J. Quantum. Electron.* **34**, pp. 336-341, 1998.

- ⁸ see, for example, L. A. Coldren and S. W. Corzine, *Diode lasers and photonic integrated circuits*, Appendix 17, Wiley, New York, 1995.
- ⁹ J. T. Olesberg, Michael E. Flatté, B. J. Brown, C. H. Grein, T. C. Hasenberg, S. A. Anson, and Thomas F. Boggess, "Optimization of active regions in mid-infrared lasers," *Appl. Phys. Lett.*, *in press*.
- ¹⁰ D. Z. Garbuzov, R. U. Martinelli, H. Lee, P. K. York, R. J. Menna, J. C. Connolly, and S. Y. Narayan, "Ultralow-loss broadened-waveguide high-power 2 μm AlGaAsSb/InGaAsSb/GaSb separate-confinement quantum well lasers," *Appl. Phys. Lett.* **69**, pp. 2006-2008, 1996.
- ¹¹ D. Z. Garbuzov, R. U. Martinelli, H. Lee, R. J. Menna, P. K. York, L. A. DiMarco, M. G. Harvey, R. J. Matarese, S. Y. Narayan, and J. C. Connolly, "4 W quasi-continuous-wave output power from 2 μm AlGaAsSb/InGaAsSb single-quantum-well broadened waveguide laser diodes," *Appl. Phys. Lett.* **70**, pp. 2931-2933, 1997.
- ¹² J. R. Lindle, J. R. Meyer, C. A. Hoffman, F. J. Bartoli, G. W. Turner, and H. K. Choi, "Auger lifetime in InAs, InAsSb, and InAsSb-InAlAsSb quantum wells," *Appl. Phys. Lett.* **67**, pp. 3153-3155, 1995.
- ¹³ M. E. Flatté, J. T. Olesberg, S. A. Anson, T. F. Boggess, T. C. Hasenberg, R. H. Miles, and C. H. Grein, "Theoretical performance of mid-infrared broken-gap multilayer superlattice lasers," *Appl. Phys. Lett.* **70**, pp. 3212-3214, 1997.
- ¹⁴ J. T. Olesberg, M. E. Flatté, T. C. Hasenberg, C. H. Grein, "Ideal performance of mid-infrared InAs/GaInSb separate confinement heterostructure laser diodes", *in preparation*.
- ¹⁵ M. E. Flatté, P. M. Young, L.-H. Peng, and H. Ehrenreich, "Generalized superlattice $\mathbf{K}\cdot\mathbf{p}$ theory and intersubband optical transitions," *Phys. Rev. B* **53**, pp. 1963-1978, 1996.
- ¹⁶ *Physics of Group IV Elements and III-V Compounds*, Landolt-Börnstein Vol. III/17a, edited by O. Madelung, Springer, New York, 1982; *Intrinsic Properties of Group IV Elements and III-V, II-VI, and I-VII Compounds*, Landolt-Börnstein Vol. III/22a, edited by O. Madelung, Springer, New York, 1987.
- ¹⁷ J. T. Olesberg, S. A. Anson, S. W. McCahon, M. E. Flatté, T. F. Boggess, D. H. Chow, and T. C. Hasenberg, "Experimental and theoretical density-dependent absorption spectra in (GaInSb/InAs)/AlGaSb superlattice multiple quantum wells," *Appl. Phys. Lett.* **72**, pp. 229-231, 1998.
- ¹⁸ C. H. Grein, P. M. Young, M. E. Flatté, and H. Ehrenreich, "Long wavelength InAs/InGaSb infrared detectors: Optimization of carrier lifetimes," *J. Appl. Phys.* **78**, pp. 7143-7152, 1995.
- ¹⁹ Michael E. Flatté, C. H. Grein, T. C. Hasenberg, S. A. Anson, D.-J. Jang, J. T. Olesberg, and Thomas F. Boggess, "Carrier recombination rates in narrow-gap InAs/Ga_{1-x}In_xSb-based superlattices," *Phys. Rev. B*, *in press*.
- ²⁰ J. T. Olesberg, Thomas F. Boggess, S. A. Anson, D.-J. Jang, M. E. Flatté, T. C. Hasenberg, C. H. Grein, "Auger recombination in antimony-based, strain-balanced, narrow-band-gap superlattices," in *Infrared Applications of Semiconductors II*, edited by D. L. McDaniel, Jr., M. O. Manasreh, R. H. Miles, and S. Sivanathan, Mater. Res. Soc. Proc. **484**, pp. 83-88, Warrendale, PA, 1998.
- ²¹ K. L. Vodopyanov, H. Graener, C. C. Phillips, and T. J. Tate, "Picosecond carrier dynamics and studies of Auger recombination processes in indium arsenide at room temperature," *Phys. Rev. B* **46**, pp. 13194-13200, 1992.
- ²² D.-J. Jang, Michael E. Flatté, C. H. Grein, J. T. Olesberg, T. C. Hasenberg, and Thomas F. Boggess, "Temperature dependence of Auger recombination in a multilayer narrow-band-gap superlattice," *Phys. Rev. B* **58**, pp. 13047-13054, 1998.
- ²³ The quantity shown in Table 2 under the heading ρ_v / ρ_c is the ratio of the occupation functions at the valence and conduction band edges at the transparency density: $f_v(E_v) / f_c(E_c)$ when $f_c(E_c) + f_v(E_v) = 1$. The ratio of the zone center masses, $(m_v / m_c)^{3/2}$, could also be used, but it does not account for the strong nonparabolicity in the valence band or the presence of multiple valence subbands.